第 XX 卷第 XX 期
XXXX 年 XX 月

红 外 与 毫 米 波 学 报
J. Infrared Millim. Waves

Vol. XX, No. XX
XX，XXXX

文章编号：1001-9014(XXXX)XX-0001-10 **DOI**：10. 11972/j. issn. 1001-9014. XXXX. XX. 001

Research on variable-speed scanning method for airborne area-array whisk-broom imaging system based on vertical flight path correction

JIN Jia-Rong[1,2]， HAN Gui-Cheng[1]， WANG Chong-Ru[1,2]， WU Ren-Fei[1,2]， WANG Yue-Ming[1,2,3*]

（1. Key Laboratory of Space Active Opto-Electronics Technology，Shanghai Institute of Technical Physics，Chinese Academy of Sciences，Shanghai 200083，China；
2. University of Chinese Academy of Sciences，Beijing，100049，China；
3. Hangzhou Institute for Advanced Study，University of Chinese Academy of Sciences，Hangzhou，310024，China）

Abstract：Airborne area-array whisk-broom imaging systems often adopt constant-speed scanning schemes. For large-inertia scanning systems，constant-speed scanning consumes a significant amount of time to complete the reversal motion，limiting the system´s adaptability to high-speed reversal scanning and restricting scanning efficiency. This study proposed a novel sinusoidal variable-speed roll scanning strategy，which reduced abrupt changes in speed and acceleration，minimizing time loss during reversals. Based on the forward image motion compensation strategy in the pitch direction，a line-of-sight（LOS）position calculation model with vertical flight path correction（VFPC）was established，ensuring that the central LOS of the scanned image remained stable on the same horizontal line，which was conducive to accurate image stitching in whisk-broom imaging. Through theoretical analysis and simulation experiments，the proposed method improved scanning efficiency by approximately 18. 6% at a 90° whisk-broom imaging angle under the same speed height ratio conditions. The new VFPC method enables wide-field，high-resolution imaging，achieving single-line LOS horizontal stability with an accuracy better than 0. 4 mrad. The research work of this thesis is of great significance to promote the further development of airborne area-array whisk-broom imaging technology toward wider fields of view，higher speed height ratios，and greater scanning efficiency.

Key words：airborne remote sensing，whisk-broom imaging，image motion，vertical flight path correction（VFPC），line-of-sight（LOS）stabilization
PACS:

基于垂直航迹校正的机载面阵摆扫成像系统变速扫描方法研究

金家融[1,2]， 韩贵丞[1]， 王崇儒[1,2]， 吴任飞[1,2]， 王跃明[1,2,3*]
（1. 中国科学院上海技术物理研究所，空间主动光电技术重点实验室，上海 200083；
2. 中国科学院大学，北京 100049；
3. 国科大杭州高等研究院，浙江 杭州 310024）

摘要：机载面阵摆扫成像系统多采用匀速扫描方案，对于大惯量的整机摆扫系统，匀速式扫描需要消耗大量时间完成换向动作，制约了高速换向扫描时的适应能力，限制了系统的扫描效率。论文提出了一种正弦型的新型变速横滚扫描策略，减小速度与加速度突变，降低换向时间损耗。基于俯仰方向的前向像移补偿策略，建立了垂直航迹校正的视轴位置计算模型，使扫描图像中心视轴稳定在同一水平线，有利于摆扫图像的准确拼接。经理论分析与仿真实验验证，在90°摆扫成像角度，相同速高比条件下，扫描效率可提高约18.6%。采用新的垂直航迹计算方法，实现了宽视场高分辨率成像，单行视轴水平稳定精度优于0.4mrad。论文研究工作对推动机载面阵摆扫成像技术向着更宽视场、大速高比、高扫描效率方向的进一步发展具有重要意义。

关　键　词：航空遥感；摆扫成像；像移；垂直航迹校正；视轴稳定

Received date：2024-10-31， **收稿日期**：2024-10-31，
Foundation items：Supported by the National Key Research and Development Program（2023YFC3107602）.

Biography：JIN Jia-Rong（1998-），male，Shenyang，China，Ph. D，Research areas involves airborne area-array scanning systems，line-of-sight stabilization systems. E-mail：jinjiarong_ucas@163. com
[*] **Corresponding author**：E-mail：wangym@mail. sitp. ac. cn

中图分类号:P237 **文献标识码**:A

Introduction

Airborne infrared electro-optical imaging technology is rapidly advancing toward wide-field and high-resolution imaging [1-3]. Common scanning methods for area-array detectors include single-pass scanning [2-3] and double-pass whisk-broom scanning [4]. To balance wide-field and high-resolution imaging under the constraints of a limited area-array, and to improve scanning efficiency for increasing effective imaging time, an increasing number of airborne cameras are adopting double-pass constant-speed whisk-broom imaging schemes [5-6]. However, under high speed-to-height ratio conditions, the scanning time per pass is shortened, requiring an increase in scanning speed, which in turn leads to increased time loss during reversals. Due to the limited peak torque output of the motors, it is difficult to further improve the scanning efficiency with this method. Therefore, to further increase effective imaging time and improve system efficiency, it is necessary to optimize the scanning strategy to minimize time loss during reversals.

Airborne imaging systems primarily rely on Position and Orientation System (POS) data to determine system orientation [7-8], with compensation applied based on positional and attitude information [9-10]. In research on forward image motion compensation during aircraft flight, some scholars have achieved promising results by employing constant-speed return-sweep compensation schemes to stabilize the LOS at the aircraft's ground projection point [11-12]. This method is straightforward and can effectively achieve track-following scanning trajectories under constant-speed whisk-broom scanning in the wingspan direction, meeting the forward overlap requirements of double-pass whisk-broom scanning. However, theoretical calculations show that the ground projection of this constant-speed return-sweep compensation trajectory forms a hyperbola. Under large forward-motion angle conditions, long single-frame exposure times can lead to image motion, resulting in blurred images. As whisk-broom imaging technology evolves toward wider fields of view and larger total scan angles, the deviations caused by this method during large-tilt-angle scans are amplified. Consequently, a new forward image motion compensation scheme is needed to meet the requirements of next-generation airborne cameras for wide-field imaging and high speed-to-height ratios.

To address the limitations of the constant-speed whisk-broom scanning scheme in terms of scanning efficiency, as well as the inapplicability of traditional constant-speed return-sweep compensation methods under variable-speed roll scanning conditions, this study proposed a novel sinusoidal variable-speed scanning strategy. This approach developed a LOS position calculation model with VFPC and incorporates forward image motion compensation, focusing on the high-accuracy compensation control curve for the pitch scanning mirror. Through software simulation modeling and hardware verification, the control curve algorithm was optimized to enhance the precision and real-time performance of the compensation, and the effectiveness of the proposed method is further validated through simulated flight imaging experiments.

1 Imaging Model of Area-Array Camera System

1.1 Imaging Principle and System Parameters

The schematic structure of the wide-field imaging system with wingspan whisk-broom scanning is shown in Fig. 1. The area-array camera is horizontally fixed on the roll gimbal, and high-resolution ground imaging is achieved through the deflection of the optical path via a reflective mirror. The pitch mirror rotates around the pitch axis to compensate for field-of-view (FOV) deviations caused by pitch attitude disturbances of the system, ensuring that the LOS during each imaging pass always points to the initial exposure position, thus providing forward motion compensation for target tracking. The roll gimbal rotates around the roll axis to compensate for FOV deviations caused by roll attitude disturbances and performs wide-field imaging in the wingspan direction. An image motion compensation mechanism is installed on the roll axis to counteract image blurring caused by wingspan scanning motion during exposure.

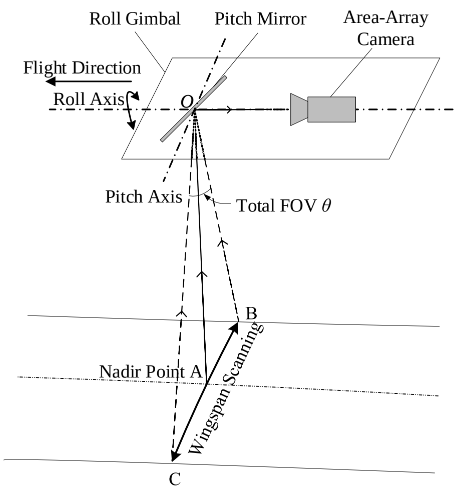

Fig. 1 Imaging structure of the whole machine with wingspan pendulum sweep
图1 整机翼展摆扫宽视场成像结构示意图

In area-array scanning imaging, FOV overlap is required to ensure seamless image stitching. The overlap occurs in both the forward flight direction and the roll wingspan direction, as illustrated in Fig. 2. The aircraft's flight altitude is H, flight speed is v, the detector has a size of $m \times n$, with an instantaneous field of view (IFOV) of β and a total FOV angle of θ.

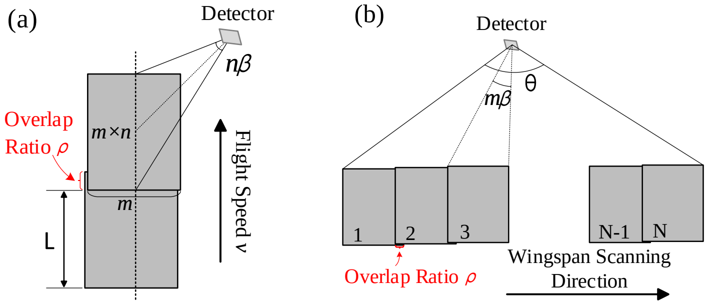

Fig.2 Schematic diagram of FOV overlap: (a)FOV overlap in flight direction; (b) FOV overlap in wingspan direction
图2 视场重叠示意图: (a)飞行方向的视场重叠; (b)翼展方向的视场重叠

The FOV overlap ratio is denoted as ρ, and during each scan, the forward flight distance of the aircraft is L, with a scan time of t. Due to time losses during the reversal motion, the scanning efficiency is η, the effective scanning time is t_{eff}, and the scanning angular velocity is ω. The expressions for these parameters are as follows:

$$\begin{aligned} & L = Hn\beta(1-\rho) \\ & t = \frac{L}{v} = n\beta(1-\rho)\frac{H}{v} \\ & t_{\mathrm{eff}} = \eta t = \eta n\beta(1-\rho)\frac{H}{v} \\ & \omega = \frac{\theta}{t_{\mathrm{eff}}} = \frac{\theta}{\eta n\beta(1-\rho)} \times \frac{v}{H} = c_1\frac{v}{H} \\ & c_1 = \frac{\theta}{\eta n\beta(1-\rho)} \end{aligned} , \qquad (1)$$

1.2 Basic Constant-Speed Scanning Strategy

1.2.1 Single-Pass Constant-Speed Scanning

The CA261 series camera, manufactured by Raytheon, uses an area-array detector for single-pass constant-speed scanning [2]. This camera is employed in reconnaissance flights under medium to low speed height ratio conditions. After each pass of constant-speed scanning, a rapid return sweep is needed to reset to the initial position, followed by acceleration to the scanning speed for the next pass.

The scan time for each pass is t, and the relationship between scanning speed and time is shown in Fig. 3(a). The green area in the figure represents the total FOV angle θ. The acceleration time from the initial position is t_1, the constant-speed scanning time is t_ω, and the acceleration during the reversal is a.

The parameter relationships for single-pass constant-speed scanning are shown in Fig. 3(b). When the angular velocity $\omega=3\theta/t$, the minimum acceleration is $a_{\min}=27\theta/t^2$, and the scanning efficiency is $\eta_{\mathrm{single}}=33\%$. The method requires a large acceleration and has low scanning efficiency.

1.2.2 Double-Pass Constant-Speed Whisk-Broom Scanning

The area-array infrared camera, independently developed by the Shanghai Institute of Technical Physics, employs a double-pass constant-speed scanning scheme [13]. Compared to single-pass constant-speed scanning, this approach eliminates the need for a rapid return sweep. In the wingspan scanning direction, only a velocity reversal is required to initiate the reverse scan, allowing the camera to capture two wide-field images in one whisk-broom cycle.

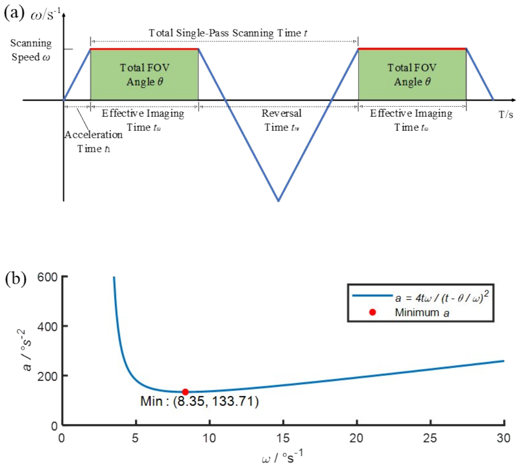

Fig. 3 Diagram of parameter relationships for single-pass constant-speed scanning: (a) Speed-time schematic diagram; (b) Acceleration-speed relationship curve
图3 单程匀速扫描参数关系图: (a)速度-时间示意图; (b)加速度-速度关系曲线

The relationship between scanning speed and time is shown in Fig. 4(a). The green area in the figure represents the total FOV angle θ.

The relationship between acceleration and scanning speed is shown in Fig. 4(b). When the angular velocity $\omega=2\theta/t$, the minimum acceleration is $a_{\min}=8\theta/t^2$, and the scanning efficiency is $\eta_{\mathrm{double}}=50\%$. When the acceleration $a=49\theta/5t^2$, the scanning efficiency increases to $\eta'_{\mathrm{double}}=71.4\%$.

For the entire whisk-broom system, further increasing the speed-to-height ratio will proportionally reduces the scan time for each pass. The motor needs to provide a torque output that increases quadratically, which complicates motor control and diminishes scanning efficiency. Therefore, it remains necessary to optimize the scanning

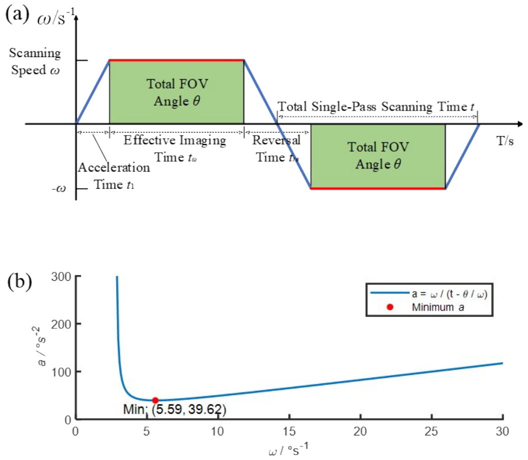

Fig. 4 Diagram of parameter relationships for double-pass constant-speed scanning: (a)Speed-time schematic diagram; (b)Acceleration-speed relationship curve
图4 双程匀速扫描参数关系图: (a)速度-时间示意图; (b)加速度-速度关系曲线

strategy.

2 Variable-Speed Whisk-Broom Strategy and Vertical Flight Path LOS Correction

2.1 Sinusoidal Variable-Speed Whisk-Broom Strategy

In response to the current system limitations, a sinusoidal double-pass variable-speed roll scanning strategy is proposed. The scan position follows a cosine curve, resulting in a sinusoidal speed curve. This eliminates abrupt changes in speed and acceleration, reducing the system's torque output requirements during scanning and thereby improving scanning efficiency. The relationship between scanning speed and time is illustrated in Fig. 5.

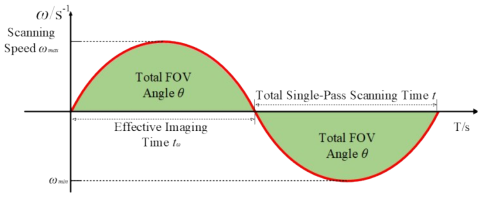

Fig. 5 Speed-time schematic diagram for double-pass variable-speed scanning
图5 双程变速扫描速度-时间示意图

The scanning motion relationship is:

$$\begin{aligned} \theta_{roll} &= \frac{\theta}{2}\sin\left(c_2\frac{v}{H}t\right) \\ \omega_{roll} &= \frac{\theta}{2}c_2\frac{v}{H}\cos\left(c_2\frac{v}{H}t\right) \\ a_{roll} &= \frac{d\omega}{dt} = \frac{\pi^2}{2}\frac{\theta}{t^2}\sin\left(c_2\frac{v}{H}t\right), \\ c_2 &= \frac{\pi}{n\beta(1-\rho)} \end{aligned} \qquad (2)$$

Where θ_{roll} is the position curve, ω_{roll} is the speed curve, and c_2 is a constant.

This variable-speed whisk-broom scheme utilizes the entire scanning process for imaging, making full use of the scan time for each pass. Considering the reset time of the forward motion mechanism, the system efficiency can reach up to 90%, which represents a further improvement compared to the double-pass constant-speed scanning scheme. The maximum acceleration amplitude is $a_{\max}=\pi^2\theta/2t$, reducing the peak acceleration by 50% and the average acceleration by approximately 70%, thereby decreasing the torque demand on the motor during reversals. This approach offers an effective solution for roll-scanning cameras under high speed-to-height ratio conditions and shows great potential for practical applications.

Compared to trapezoidal wave control, sinusoidal wave-driven current is smoother, consisting primarily of fundamental wave currents without high-frequency harmonic components. This reduces fundamental wave copper loss by 38.2% and also lowers hysteresis losses. As a result, total power consumption is reduced by approximately 60%, effectively addressing motor heating limitations.

2.2 Combined Vertical Flight Path and LOS Correction Model

Double-pass whisk-broom scanning requires coordination between forward image motion compensation in the flight direction and vertical flight path correction in the wingspan direction. Without this, adjacent images will have no overlapping areas, resulting in a step-like overall image, which hinders subsequent stitching, as shown in Fig. 6. The trajectory deviation can be divided into forward image motion deviation in the flight direction and scanning trajectory deviation in the wingspan direction.

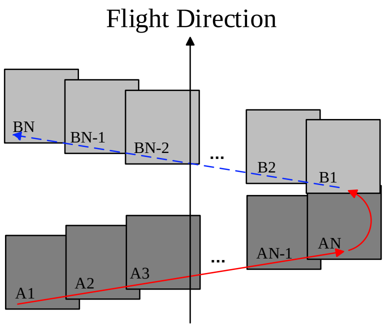

Fig. 6 Imaging schematic diagram without image motion compensation in the flight direction
图6 无飞行方向像移校正的成像示意图

2.2.1 Image Motion in the Flight Direction

The generation and compensation principle of trajectory deviation in the flight direction is illustrated in Fig. 7. The rectangular box represents a simplified system, where the pitch mirror can rotate around the pitch axis to redirect the optical path for ground imaging. When the aircraft is directly above the ground point, the pitch mirror is tilted at an angle of 45°. As the aircraft moves forward, the pitch mirror moves in the opposite direction to maintain the LOS stable at the nadir point.

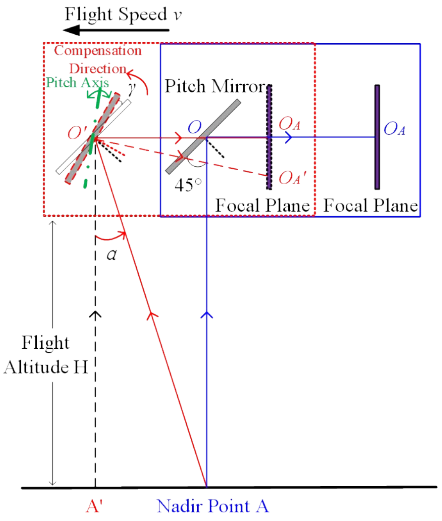

Fig. 7 Principle diagram of image motion compensation in the flight direction
图 7 飞行方向像移校正原理图

2.2.2 Scanning Deviation in the Wingspan Direction

The scanning trajectory deviation in the wingspan direction is shown in Fig. 8. When the system performs whisk-broom motion under a large FOV, the actual ground projection of the LOS shows significant variation relative to the flight altitude. In the traditional scheme [4], forward image motion compensation results in the LOS landing on a conical surface with a radius equal to the flight altitude H. When the forward tilt angle is small, the ground projection of the LOS is near the horizontal line. However, as the forward tilt angle increases, the ground projection deviates significantly from the vertical flight path, with the deviation becoming more pronounced as the scan angle increases. The solid line in the figure represents the hyperbolic trajectory of the scan path, indicating the need for a revised compensation strategy.

2.2.3 Design of the Combined LOS Path Correction

Considering the half-cycle motion, the scanning system begins its wingspan direction sweep from the aircraft directly above point A and scans half of the total FOV angle along the vertical flight path, reaching the maximum FOV angle A' on one side. The relationship between the scan angle $\Phi(t)$ and time is given by Equation (2). In the flight direction, the system moves forward at speed v, traveling from the starting point O to O' over time t. The aircraft's flight altitude is H, and the pitch mirror rotates around the pitch axis to perform corrective compensation, stabilizing the LOS along the x-axis of the vertical flight path. From the FOV angle Φ, the actual height H' from the camera to the scan point can be calculated, which in turn provides the actual LOS deviation angle α.

The expressions for the scan angle Φ, actual height H', and LOS deviation angle α are as follows:

$$\begin{aligned} \Phi(t) &= \frac{\theta}{2}\sin\left(c_2\frac{v}{H}t\right) \\ H(t)' &= \frac{H}{\cos\Phi(t)} \\ \alpha(t) &= \arctan\left(\frac{vt}{H(t)'}\right) = \arctan\left(\frac{v}{H}\cos\Phi t\right) \\ &= \arctan\left\{\frac{v}{H}t\cos\left[\frac{\theta}{2}\sin\left(c_2\frac{v}{H}t\right)\right]\right\} \end{aligned}, \quad (3)$$

According to the principle of optical reversibility, during the scanning cycle, controlling the pitch mirror to perform a reverse compensation of $\alpha/2$ around the pitch axis can stabilize the LOS along the vertical flight path for scanning motion.

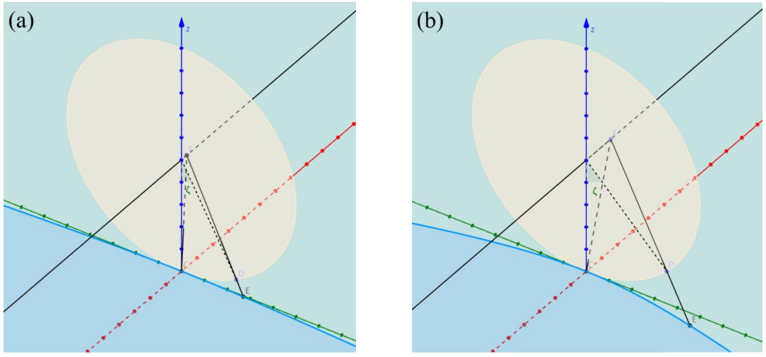

Fig. 8 Schematic diagram of track deviation in wingspan direction scanning: (a) Small forward tilt angle condition; (b) Large forward tilt angle condition
图 8 翼展方向扫描航迹偏差示意图: (a)小前向倾角条件; (b)大前向倾角条件

The expressions for the pitch compensation angle γ and compensation speed are as follows:

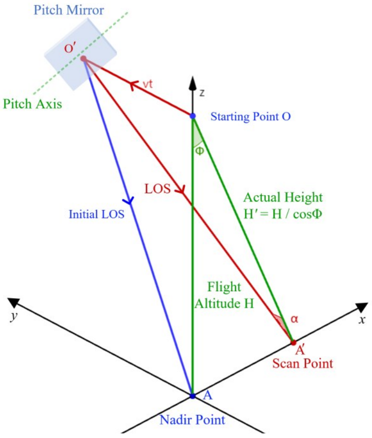

Fig. 9 Principle diagram of combined vertical track correction
图9 联合垂直航迹校正原理图

$$
\begin{aligned}
&\gamma(t) = \frac{1}{2}\alpha(t) = \frac{1}{2}\arctan\left\{\frac{v}{H}t\cos\left[\frac{\theta}{2}\sin\left(c_2\frac{v}{H}t\right)\right]\right\} \\
&\omega_{pitch}(t) = \frac{d\gamma(t)}{dt} = \frac{1}{1+\left\{\frac{v}{H}t\cos\left[\frac{\theta}{2}\sin\left(c_2\frac{v}{H}t\right)\right]\right\}^2}\cdot \\
&\left\{\frac{v}{H}\cos\left[\frac{\theta}{2}\sin\left(c_2\frac{v}{H}t\right)\right] - c_2\left(\frac{v}{H}\right)^2 t\sin\left[\frac{\theta}{2}\sin\left(c_2\frac{v}{H}t\right)\right]\frac{\theta}{2}\cos\left(c_2\frac{v}{H}t\right)\right\}
\end{aligned}
\quad , \tag{4}
$$

According to Equation (4), the position and speed functions of the pitch compensation mirror involve nested trigonometric functions, leading to high computational complexity and significant hardware resource consumption. In hardware implementations, both the position loop and speed loop require complex trigonometric calculations, which occupy considerable hardware resources and hinder real-time compensation. Therefore, simplifications and approximations are needed to reduce the complexity of the control algorithm and achieve efficient compensation.

By performing a polynomial expansion and approximation optimization on the trigonometric functions such as arctan in the LOS deviation angle α, and ignoring higher-order terms beyond the 7th order, the following is obtained:

$$
\begin{aligned}
&\alpha(t) = \frac{v}{H}t - \frac{1}{8}\theta^2 c_2{}^2\left(\frac{v}{H}\right)^3 t^3 + \frac{1}{24}\theta^2 c_2{}^4\left(\frac{v}{H}\right)^5 t^5 - \frac{1}{602}\theta^4 c_2{}^6\left(\frac{v}{H}\right)^7 t^7 + O(t^9) \\
&\omega_{pitch}(t) = \frac{1}{2}\frac{d\alpha(t)}{dt} = \frac{v}{H} - \frac{3}{8}\theta^2 c_2{}^2\left(\frac{v}{H}\right)^3 t^2 + \frac{5}{24}\theta^2 c_2{}^4\left(\frac{v}{H}\right)^5 t^4 - \frac{1}{86}\theta^4 c_2{}^6\left(\frac{v}{H}\right)^7 t^6 + O(t^8)
\end{aligned}
\quad , \tag{5}
$$

Considering only the approximation error in the compensation algorithm, the optimized compensation function yields a LOS correction deviation of less than 0.5% at a maximum scan angle of 40°, and less than 0.8% globally, achieving precise vertical flight path correction. Compared to the nested trigonometric function approach for exact calculations, this scheme simplifies the process using a polynomial expansion, significantly reducing the control complexity in both the position loop and speed loop of the control system, thereby improving the system's real-time performance.

3 Experimental Verification and Discussions

A half-cycle simulation was selected to verify the accuracy of the correction path algorithm. The correction algorithm path, as compared to the theoretical position curve, was presented in Fig. 13(a), while the deviation curve was shown in Fig. 13 (b). The correction algorithm's compensation deviation was on the order of 10^{-4} compared to the theoretical curve. Under an instantaneous FOV of 250 μrad, the overall deviation was better than 1.8 pixels. During a single frame exposure time of 10 ms, the maximum deviation angle was 9.8×10^{-5} rad, which was better than 0.4 pixels, meeting the requirements for LOS compensation.

On the hardware platform, a single-step simulation was used to compare the optimized LOS path algorithm proposed in this study with the CORDIC algorithm. The time difference between the end of the calculation and the reset point was used as the single-step computation time. At t = 0.15s, the theoretical LOS position was

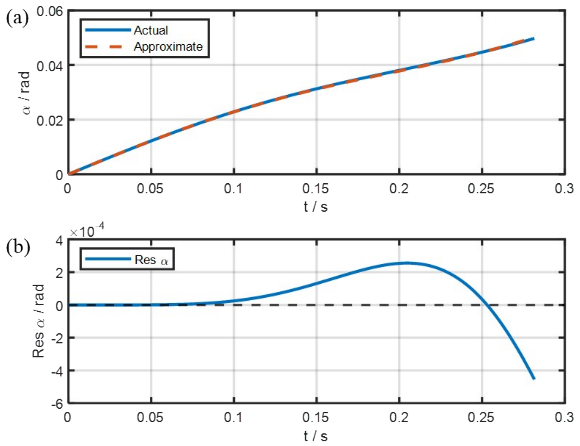

Fig. 10 Correction algorithm curve and theoretical position curve: (a) Angle curve; (b) Residual curve
图10 校正算法曲线与理论位置曲线：(a)角度曲线；(b)偏差曲线

0.03129 rad, while the calculated value from the proposed LOS correction algorithm was 0.03125 rad, with a deviation of 40 μrad and a computation time of 75 ns. In comparison, the CORDIC algorithm calculated the position as 0.03137 rad, with a deviation of 80 μrad and a computation time of 645 ns. The proposed method reduced the computation time by an order of magnitude, benefiting real-time compensation.

The LOS correction effect and the fitted curve at different time points were shown in Fig. 11. The fitted curve aligned well with the simulation curve, with an error ranging from -0.4 mrad to 0.4 mrad. The computation time per step was consistently 75 ns, enabling LOS correction and compensation for the vertical flight path.

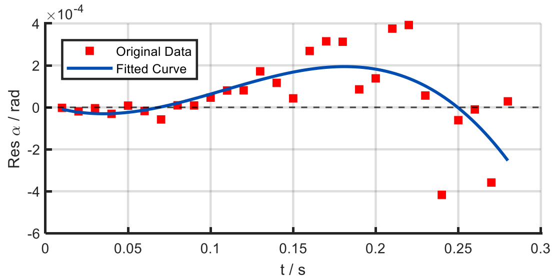

Fig. 11 Correction effect of LOS
图11 视轴校正效果

A long-focus pod camera with a single-frame FOV of 9.33°×9.33° was used as the experimental subject. A visible light area-array camera with the same technical specifications was used to replace the area-array infrared camera for functionality verification. The camera achieved 70° wide-field coverage through seven exposures. The equipment was mounted on a simulated flight test platform for imaging experiments, using the aircraft’s actual attitude variation curve within a single flight strip as input, as shown in Fig. 12. The pointing commands were superimposed and compensated using attitude information feedback from the POS.

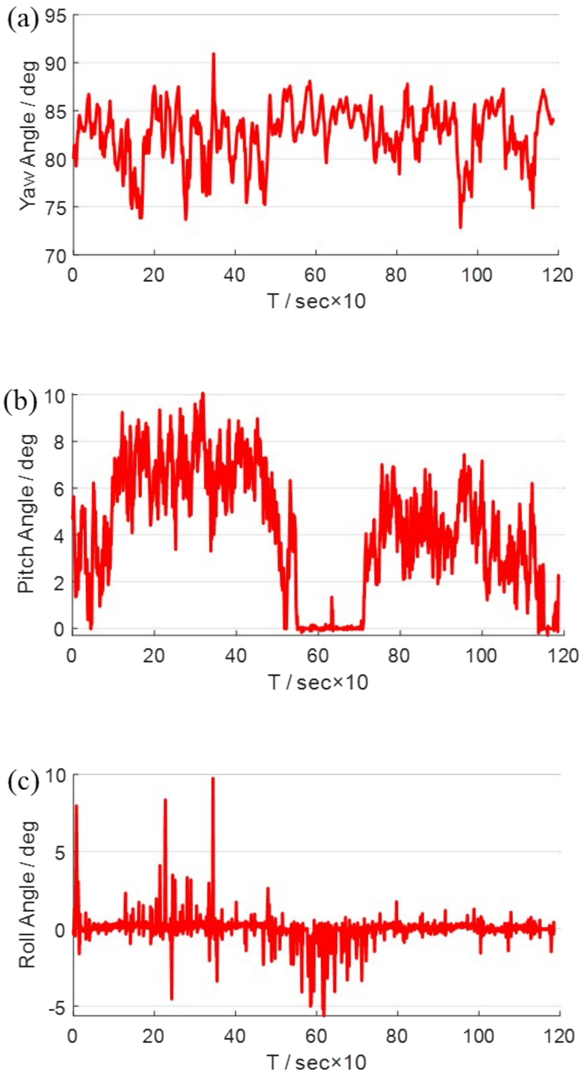

Fig. 12 Aircraft attitude angle change curves: (a)Yaw; (b)Pitch; (c)Roll
图 12 载机姿态角度变化曲线: (a)方位角; (b)俯仰角; (c)横滚角

The comparison of imaging results for the forward-pass and return-pass scans were shown in Figs. 13 and 14. The dashed rectangular box represented the FOV for a single image, with the center of the rectangle being the LOS center. The solid rectangular box indicated the stitching alignment area, which remained consistent for both methods. In the traditional method, the maximum LOS deviation between the first and last frames of each scan pass was 29 pixels, corresponding to 0.39°. In contrast, the new method proposed in this study reduced the maximum deviation to 5 pixels, corresponding to 0.07°. The central LOS remained essentially aligned with the horizontal line of the vertical flight path, confirming the effectiveness of the vertical flight path LOS correction method proposed in this study.

The LOS pointing deviations for the two scanning methods illustrated above were shown in Table 1, where (a)~(g) correspond to the exposure sequence of the seven images. The center of the FOV for the center exposure image (d) was selected as the horizontal LOS reference point for each row of images. With this method, the root mean square (RMS) of the central LOS stability deviation was improved from 9.23 pixels, as seen in the traditional method, to 2.78 pixels.

From the data in the Table 1, it was observed that using the new vertical flight path correction method, the exposure images near the center point of each image row showed pixel errors relative to the horizontal axis ranging from 1 to 2 pixels, corresponding to 0.25 ~ 0.5 mrad. For exposure images located at the boundary of a single row (roll angle $\Phi = 30^\circ$), the vertical deviation relative to the central horizontal axis was approximately 4 pixels, corresponding to 1 mrad. In the previously discussed simulation of the optimized algorithm, the error near the central exposure point was approximately 0.2 mrad, while the error near the boundary of a single row was 0.4 mrad. The comparison indicated that during the simulated flight imaging experiments, a system error of approximately 0.6 mrad still existed.

The traditional algorithm did not account for changes in actual imaging elevation caused by roll rotation. Compared with the new vertical flight path algorithm, the pitch angle of the camera in the traditional algorithm differed by a factor of the cosine of the roll angle. As a result, the imaging position gradually deviated from the horizontal flight path as the roll angle increases, with cumulative errors observed. This trend aligned with the incremental pixel error shown in the Table 1. Considering

Table 1 LOS Stability Deviation in Area-Array Imaging Systems

表1 面阵成像系统视轴稳定偏差

Method		Deviation (px)							RMS
		(a)	(b)	(c)	(d)	(e)	(f)	(g)	
Traditional	forward-pass	−14	−9	−2	0	3	9	15	9.23
	return-pass	14	10	2	0	−3	−8	−14	9.02
New	forward-pass	−2	0	−2	0	−1	−2	−5	2.33
	return-pass	4	2	1	0	1	4	4	2.78

Fig. 13 Comparison of imaging effects during forward-pass scanning: (a)Traditional method; (b)New method
图13 去程扫描成像效果对比:(a)传统方法;(b)新方法

Fig. 14 Comparison of imaging effects during return-pass scanning: (a)Traditional method; (b)New method
图14 回程扫描成像效果对比:(a)传统方法;(b)新方法

the exposure position at the boundary of a single row with a roll angle of $\Phi = 30^\circ$, the pitch compensation angle for the new algorithm was $\alpha_1 = 0.04$ rad. In contrast, for the traditional algorithm, after applying a slow factor of $n = 0.93$, the pitch compensation angle was calculated as $\alpha_2 = \alpha_1 / (n\cos\Phi) = 0.043$ rad. The compensation deviation in this case was 3 mrad, corresponding to 12 pixels. Comparing this result with the data in Table 1, a system error of 2 pixels, equivalent to 0.5 mrad, was observed.

In the experimental model used in this study, system errors were classified into random errors, measurement errors, control errors, and stitching errors. Since the POS attitude was a known input under experimental conditions, the random error was attributed to the synchronization attitude error of the attitude simulation platform. The measurement error originated from the encoder feedback error, with the encoder system employing a 26-bit absolute encoder that achieved an accuracy of 0.058 mrad. Control error referred to the pointing error of the servo motor, which could result in certain delay errors due to the computation cycle and servo delay. As the primary objective of this experiment was to verify the control path planning of the LOS center point, no post-processing was applied to the images, and only simple stitching was performed. Due to edge field distortion in area-array imaging, a stitching error was also present, which was calculated as 1 pixel, equivalent to 0.25 mrad. In summary, the servo control mechanism introduced approximately 0.2 mrad of control error. This could be further improved in future study to enhance the pointing accuracy of the LOS.

The 70° wide-field imaging effect based on vertical flight path LOS compensation was shown in Fig. 15. The system delivered good imaging performance, with rich image information and clearly discernible target details. Due to the simple stitching applied to the images, some geometric distortions were observed in the buildings, but the central FOV exhibited good overlap.

As with the majority of studies, the current study was subject to limitations. The combined correction LOS path design proposed in this study weas based on the assumption that all imaging rows were at the same ground elevation. This strategy was less applicable to steep mountainous terrains with significant ground elevation variations. If the ground elevation changed significantly within an imaging row, a corresponding scanning strategy would need to be designed based on the actual terrain.

4 Conclusions

To address the efficiency limitations of current wide-field, high-resolution imaging systems during high-speed reversals, this study proposed a novel sinusoidal variable-speed whisk-broom scanning scheme. This method utilized the entire scanning time for imaging, improving time efficiency by approximately 18.6% compared to constant-speed whisk-broom scanning. To solve the problem of forward constant-speed image motion compensation being unsuitable for large forward tilt angles and large scan FOV angles, a forward image motion compensation strategy based on vertical flight path correction was proposed. The compensation curve calculation was optimized to enhance computational efficiency, achieving a LOS compensation accuracy better than 0.4 mrad. Using an area-array camera on a simulated flight test platform, an external imaging experiment was conducted to verify the feasibility of the variable-speed scanning method and vertical flight path LOS correction. The experiment produced wide-field, high-resolution images with a stable horizontal LOS. This research is of great significance for advancing airborne whisk-broom imaging technology towards wider fields of view, higher speed-to-height ratios, and higher resolutions.

Fig. 15 Wide-field imaging based on vertical flight path LOS compensation
图15 基于垂直航迹视轴补偿的宽视场成像效果

References

[1] WANG C R, YANG L F, CAO X, et al. Recent progress of airborne infrared remote sensing technology in SITP[J]. J. Infrared Millim. Waves, 2022, 41(1): 007.

[2] Lareau A G. Flight demonstration of the CA-261 step frame camera [C]. Proceedings Volume 3128, Airborne Reconnaissance XXI. Optical Science, Engineering and Instrumentation '97, 1997, San Diego, CA, United States: SPIE, 1997: 17-28.

[3] PANG Y, LIANG X J, JIA W, et al. The Comprehensive Airborne Remote Sensing Experiment In Saihanba Forest Farm[J]. National Remote Sensing Bulletin, 2021, 25(4): 14.

[4] Iyengar M, Lange D. The Goodrich 3rd generation DB-110 system: operational on tactical and unmanned aircraft[C]. Proceedings Volume 6209, Airborne Intelligence, Surveillance, Reconnaissance (ISR) Systems and Applications III. Defense and Security Symposium, 2006, Orlando (Kissimmee), Florida, United States: SPIE, 2006: 620909.

[5] WANG C R, HAN G C, JIN X B, et al. A new method for LOS path planning and overlap rate setting of airborne area-array whisk-broom imaging[J]. J. Infrared Millim. Waves, 2023, 42(03): 383-390.

[6] LI S, HU Y, GONG C L, et al. A step-by-step geometric correction and error analysis of swing-swept array thermal infrared aerial image [J]. J. Infrared Millim. Waves, 2020, 39(2): 242~250.

[7] QIAO C, DING Y L, XU Y S, et al. Ground target geo-location using imaging aerial camera with large inclined angle[J]. Optics and Precision Engineering, 2017, 25(07): 1714-1726.

[8] DU Y L, DING Y L, XU Y S, et al. Geo-Location Algorithm for TDI-CCD Aerial Panoramic Camera[J]. Acta Optica Sinica, 2017, 37(03): 355-365.

[9] WANG Y K, HAN G C, QI H X, et al. Investigation of image motion compensation technique based on real-time LOS tracking[J]. J. Infrared Millim. Waves, 2015, 34(6): 0757.

[10] Hong S Y, Wang Y K, Han G C, et al. Study on Real-Time LOS Stabilization Technique Based on Dual Reflectors in the Airborne Remote Sensing Imaging System[J]. Aero Weaponry, 2020, 27(5): 86-90.

[11] LIU Y B, WANG Y K, HAN G C, et al. Aviation wide field thermal imaging technology based on array detector sweep-stop pattern[J]. J. Infrared Millim. Waves, 2017, 36(3): 330~335.

[12] JIANG B, GE M F, LIU M, et al. Research on image stabilization technology of area-array aerial camera[J]. Infrared and Laser Engineering, 2014, 43(10): 3467-3473.

[13] WANG Y K, QI H X, HAN G C, et al. Study on light-small whiskbroom scanning thermal imaging system with area-array detector[J]. Laser & Infrared, 2017, 36(3): 330~335.